Monthly Notices
of the
ROYAL ASTRONOMICAL SOCIETY

MNRAS **495,** 2446–2457 (2020)
Advance Access publication 2020 May 8

doi:10.1093/mnras/staa1283

Photometry and performance of SPECULOOS-South

C. A. Murray,[1]★ L. Delrez,[1] P. P. Pedersen,[1] D. Queloz,[1] M. Gillon,[2] A. Burdanov,[2] E. Ducrot,[2] L. J. Garcia,[2] F. Lienhard,[1] B. O. Demory,[3] E. Jehin,[4] J. McCormac,[5,6] D. Sebastian,[2] S. Sohy,[4] S. J. Thompson,[1] A. H. M. J. Triaud,[7] V. V. Grootel,[4] M. N. Günther[8]† and C. X. Huang[8]†

[1]*Cavendish Laboratory, JJ Thomson Avenue, Cambridge CB3 0HE, UK*
[2]*Astrobiology Research Unit, Université de Liège, Allée du 6 Août 19C, B-4000 Liège, Belgium*
[3]*University of Bern, Center for Space and Habitability, Sidlerstrasse 5, CH-3012 Bern, Switzerland*
[4]*Space Sciences, Technologies and Astrophysics Research (STAR) Institute, Université de Liège, Allée du 6 Août 19C, B-4000 Liège, Belgium*
[5]*Centre for Exoplanets and Habitability, University of Warwick, Gibbet Hill Road, Coventry CV4 7AL, UK*
[6]*Department of Physics, University of Warwick, Gibbet Hill Road, Coventry CV4 7AL, UK*
[7]*School of Physics and Astronomy, University of Birmingham, Edgbaston, Birmingham B15 2TT, UK*
[8]*Department of Physics, and Kavli Institute for Astrophysics and Space Research, Massachusetts Institute of Technology, Cambridge, MA 02139, USA*

Accepted 2020 May 4. Received 2020 May 2; in original form 2019 October 28

ABSTRACT

SPECULOOS-South, an observatory composed of four independent 1-m robotic telescopes, located at ESO Paranal, Chile, started scientific operation in 2019 January. This Southern hemisphere facility operates as part of the Search for Habitable Planets EClipsing ULtra-cOOl Stars (SPECULOOS), an international network of 1-m-class telescopes surveying for transiting terrestrial planets around the nearest and brightest ultracool dwarfs (UCDs). To automatically and efficiently process the observations of SPECULOOS-South, and to deal with the specialized photometric requirements of UCD targets, we present our automatic pipeline. This pipeline includes an algorithm for automated differential photometry and an extensive correction technique for the effects of telluric water vapour, using ground measurements of the precipitable water vapour. Observing very red targets in the near-infrared can result in photometric systematics in the differential light curves, related to the temporally-varying, wavelength-dependent opacity of the Earth's atmosphere. These systematics are sufficient to affect the daily quality of the light curves, the longer time-scale variability study of our targets and even mimic transit-like signals. Here we present the implementation and impact of our water vapour correction method. Using the 179 nights and 98 targets observed in the $I + z'$ filter by SPECULOOS-South since 2019 January, we show the impressive photometric performance of the facility (with a median precision of ∼1.5 mmag for 30-min binning of the raw, non-detrended light curves) and assess its detection potential. We compare simultaneous observations with SPECULOOS-South and *TESS*, to show that we readily achieve high-precision, space-level photometry for bright, UCDs, highlighting SPECULOOS-South as the first facility of its kind.

Key words: atmospheric effects – techniques: photometric – planets and satellites: detection.

1 INTRODUCTION

The search for extra-terrestrial life is one of the greatest challenges in modern-day astronomy, driven by the question: are we alone in the Universe? A promising path to an answer is to search for temperate Earth-sized exoplanets in order to probe their atmospheres for biosignatures with next-generation telescopes, such as the *James Webb Space Telescope* (Gardner et al. 2006) and future Extremely Large Telescopes (e.g. Gilmozzi & Spyromilio 2007; Sanders 2013).

The case for ultracool dwarf (UCD) hosts is compelling as we move towards detecting Earth-sized, temperate worlds. UCDs are Jupiter-sized objects of spectra-type M7 and later, with effective

★ E-mail: cam217@cam.ac.uk
† Juan Carlos Torres Fellow.

temperatures cooler than 2700 K (Kirkpatrick 2005). Compared to a Sun-like host, temperate planets around UCDs have more frequent transits, there is a higher geometric probability of observing the transit, and transit depths are two orders of magnitude deeper (Earth-radius planets orbiting UCDs have transit depths of ∼1 per cent). Due to their low luminosities and small sizes, the detection of spectroscopic signatures in the atmosphere of a temperate terrestrial planet is also more favourable for UCDs than any other host star (Kaltenegger & Traub 2009; Seager, Deming & Valenti 2009; de Wit & Seager 2013). Despite being numerous in our local stellar neighbourhood (Kirkpatrick et al. 2012), there remain many unanswered questions about UCDs, including a lack of statistics on their planet population (Delrez et al. 2018). These gaps in our knowledge, as well as the discovery of seven transiting Earth-sized exoplanets in temperate orbits of 1.5–19 d around TRAPPIST-1 (Gillon et al. 2016, 2017) helped to strengthen the case for a survey performing dedicated photometric monitoring of UCDs, Search for Habitable Planets EClipsing ULtra-cOOl Stars (SPECULOOS; Burdanov et al. 2018; Delrez et al. 2018; Gillon 2018), and has motivated the development of future UCD surveys (e.g. Tamburo & Muirhead 2019).

While the photometric precisions reached by ground-based transit surveys has improved dramatically over the past 20 yr, these facilities are not yet able to detect the shallow 0.01 per cent transit depths produced by an Earth-radius planet orbiting a Sun-like host. Limited by the Earth's rapidly changing weather and atmospheric conditions, current state-of-the-art facilities, such as Next Generation Transit Search (NGTS; Wheatley et al. 2018) and SPECULOOS-South, are able to reach photometric precisions of 0.1 per cent. Ground-based transit surveys have previously shown a trade-off between two factors; the size of detectable planet and the photometric quality. While observing Sun-like objects in the visible reduces the systematics caused by the Earth's atmosphere, it limits the smallest detectable planets to Neptune-sized. On the other hand, observing redder objects, such as mid-to-late M-dwarfs, which are faint in the visible and therefore must preferentially be observed in the infrared (IR) or near-IR, allows for the detection of super-Earth and Earth-sized planets. Observing these objects, however, comes with significant challenges. The stellar variability and common flares (Williams et al. 2015; Gizis et al. 2017; Günther et al. 2019) of low-mass red dwarfs can complicate the detection of transiting planets. In addition, in the near-IR, the varying wavelength-dependent opacity of the Earth's atmosphere has significant effects on the incoming light. Specifically, second-order extinction effects due to highly variable absorption by atmospheric water vapour have previously limited the quality of the photometry for red dwarfs, as experienced by MEarth (Berta et al. 2012). In this paper, we present a method of modelling and correcting the effect of precipitable water vapour (PWV) during differential photometry. Not only does this correction eliminate the chance of spurious transit-like signals caused by short time-scale changes in PWV, but it significantly reduces the red noise in the photometry.

The SPECULOOS survey is a network of 1-m-class robotic telescopes searching for transiting terrestrial planets around the nearest and brightest UCDs. The main facility of the network in the Southern hemisphere, the SPECULOOS-South Observatory (SSO), started full scientific operations in 2019 January at the ESO Paranal Observatory (Chile). The SPECULOOS-North Observatory (SNO) based at the Teide Observatory in Tenerife (Canary Islands) is currently being developed and saw the first light of its first telescope in 2019 June. Along with contributions from SAINT-EX in San Pedro Mártir (Mexico), TRAPPIST-South at ESO's La Silla Observatory (Chile), and TRAPPIST-North at the Oukaïmeden Observatory (Morocco) (Gillon et al. 2011; Jehin et al. 2011), these observatories will work together to observe around approximately 1200 of the nearest and brightest UCDs. Over the course of the next 10 yr, this survey will allow us to determine the frequency and diversity of temperate terrestrial planets around low-mass objects and will provide first-class targets for further atmospheric study in the search for signs of habitability beyond the Solar system.

The SSO aims to detect single transits from Earth-sized planets, requiring photometric precisions of ∼0.1 per cent. To obtain the necessary high signal-to-noise ratio (S/N) light curves, and to deal with the specificity of our very red targets, we developed a specialized automatic pipeline to process and reduce the data from the SSO. This pipeline includes a novel differential photometry algorithm and a correction of the effects of variable telluric water absorption. Since the start of scientific operations, we have been tracking the quality of the SSO's photometry. This provides feedback into the photometric pipeline and allows us to assess whether the facility is reaching the expected performances set out by the survey goals. This paper details the various stages involved in assessing SSO's performance during its first year of operation: a description of the SPECULOOS-South Pipeline in Section 3, the differential photometry technique developed in Section 4, the impact of telluric water vapour on photometry, and an outline of the implemented correction in Section 5, and the determination of the overall photometric performance of the survey in Section 6.

2 THE SPECULOOS-SOUTHERN OBSERVATORY

The SSO consists of four robotic 1-m Ritchey–Chretien telescopes,[1] each equipped with a deeply depleted CCD detector that is optimized for the near-IR. For the vast majority of our observations we use the $I + z'$ custom-designed filter (transmittance >90 per cent from 750 nm to beyond 1000 nm) due to the faintness of our red targets in the optical wavelength domain. However, we are limited beyond 950 nm by the quantum efficiency of our CCD detector. Further technical information is shown in Table 1 and described in more detail, alongside transmission curves [fig. 7 for the $I + z'$ filter transmission curve and fig. 6 (right-hand side) for the total efficiency in $I + z'$], in Delrez et al. (2018).

Observations on the four telescopes are started remotely each night. Each telescope operates independently and in robotic mode following plans written by SPECULOOS's automatic scheduler. On average, one to two targets are observed by each telescope per night. Each target will be observed continuously for between several hours and an entire night (for, however, long weather permits and the target is observable). Typically, we observe each target between one and two weeks, depending on its spectral type, so as to efficiently probe the temperate region around that object. As this is a targeted survey, our targets are spread over the sky, therefore there is only one target per field of view (FOV). During operation, each telescope uses the auto-guiding software, DONUTS (McCormac et al. 2013), to calculate real-time guiding corrections and to re-centre the telescope pointing between exposures. Systematic errors caused by

[1]The SSO telescopes are named after the four Galilean moons: Europa, Io, Callisto, and Ganymede. This is partially because this Jovian system mirrors the size ratio between Earth-sized planets and their UCD host, but also as a tribute to the first objects discovered to orbit a body other than the Earth, challenging the geocentric Ptolemaic model of the time.

Table 1. Technical specifications of each telescope in the SSO.

	Specification
Mirrors	1-m-diameter primary with a *f*/2.3 focal ratio and 28-cm diameter secondary; combined *f*/8 focal ratio; both mirrors are coated with pure aluminium
Camera	Andor iKon-L thermoelectrically cooled camera
CCD detector	Near-IR-optimized deeply depleted 2k × 2k e2v CCD detector
CCD quantum efficiency	∼350 (near-UV) to ∼950 nm (near-IR); peak quantum efficiency of 94 per cent at 740 nm
Field of view	12×12 arcmin^2
Pixel scale	0.35 arcsec pixel^{-1}
Pixel size	13.5 µm
Dark current	∼0.1 e$^-$ s^{-1} pixel^{-1} when the camera is operated at −60°C
Readout mode	Usually 1-MHz readout mode with a pre-amplifier gain of 2 e$^-$ ADU^{-1} providing readout noise of 6.2 e$^-$
Gain	1.04 e$^-$ ADU^{-1}
Filter wheel	Finger Lakes Instrumentation (model CFW3-10) allowing ten 5 cm x 5 cm filters
Filters	All telescopes: Sloan g', r', i', z, $I+z'$, 'blue-blocking' filters; selected telescopes: broad-band Johnson–Cousins B, R_C, and V filters, and the Sloan u' filter

the drift of stars on the CCD (with inhomogeneous pixel response) can severely limit the precision of time-series photometry; therefore, fixing stellar positions at the sub-pixel level is essential. DONUTS is also capable of auto-guiding on defocused stars, which is useful, for example, when we observe bright objects.

All raw images recorded by the facility are automatically uploaded at the end of the night to the online ESO archive.[2] These images are then automatically downloaded to a server at the University of Cambridge (UK), and analysed by the pipeline. All images (and extracted light curves of all objects observed in all fields) will be made publicly available after a 1-yr proprietary period.

3 THE SPECULOOS-SOUTH PIPELINE

Every survey presents unique calibration and photometric challenges and so we have developed a pipeline specific for SSO. We designed this photometric pipeline to be fast, automatic, and modular. Depending on the targets and conditions of the night, we accumulate approximately between 250 and 1000 images per telescope per night with typical exposure times of 10–60 s, corresponding to between 4 and 16 GB of data. Flexibility in the pipeline allows us to perform various quality checks, extract feedback, and use these to optimize the performance of the survey. Modularity allows reprocessing certain stages of the pipeline with improved algorithms, without requiring a full re-run.

The structure and data format of the SSO pipeline is based on the architecture of the NGTS pipeline described in Wheatley et al. (2018). Similarly to NGTS, we built our pipeline on top of the CASUTOOLS[3] package of processing tools for image analysis, astrometric fitting, and photometry (Irwin et al. 2004).

The various steps of the pipeline are illustrated in Fig. 1. The science images are calibrated through bias and dark subtraction and flat-field division (Section 3.1). Astrometric solutions are found for each image (Section 3.2). If this is the first night of observation for a given field, then these images are aligned and stacked to create a stacked image. Sources detected on this stacked image are used to generate a catalogue of stars for this FOV (Section 3.3). Precise aperture photometry measurements are extracted from each image using the catalogue with a selection of different aperture sizes (Section 3.4). We can then generate differential light curves for any object in the catalogue: either for a single night or over many nights to assemble a 'global' light curve (Section 4). Global light curves can be used to assess the photometric variability of a target over multiple nights. Systematic effects, such as those caused by changes in PWV, are then removed (Section 5).

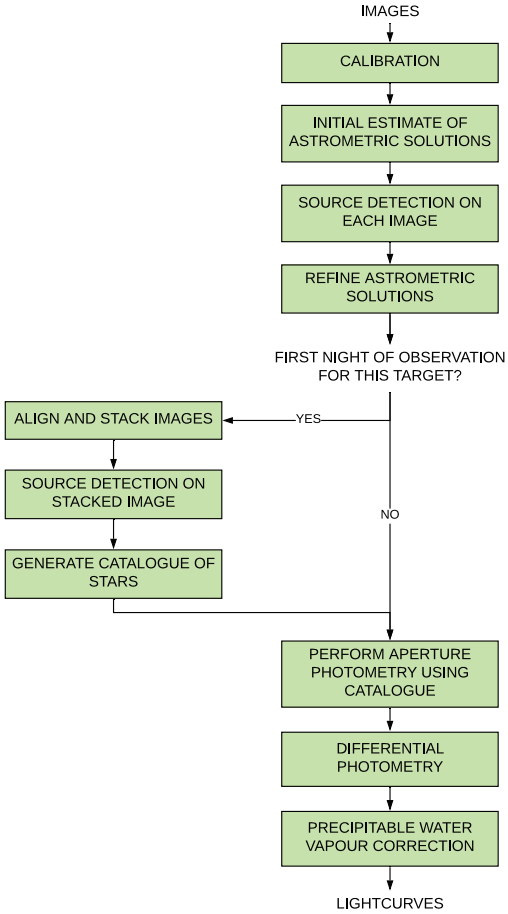

Figure 1. Simplified flowchart of the SPECULOOS-South pipeline.

3.1 Data reduction

Standard methods of bias and dark subtraction and flat-field correction are used to calibrate the science images. Bias and dark images are taken at dawn, after the closure of the telescope dome, whereas the flat-field images are captured using the twilight sky at both dusk and dawn. All images are overscan subtracted and the bias, dark, and flat-field frames are σ-clipped and median-combined to produce master calibration images, with appropriate corrections using the other master calibration images. The master flat images are monitored over time to assess their quality and flag significant variations (e.g. moving dust). These master calibration images are then used to calibrate the science images.

[2] http://archive.eso.org/eso/eso_archive_main.html.
[3] http://casu.ast.cam.ac.uk/surveys-projects/software-release.

3.2 Astrometry

Despite good performance of the telescope guiding with DONUTS, there remain very small drifts in object positions during the night, of the order of ∼0.1 arcsec (∼0.3 pixels). Precise astrometric solutions are needed for each image to accurately place apertures for photometric measurements. A local version of ASTROMETRY.NET code (Lang et al. 2010) is used to cross-match each science image with reference catalogues built from the 2MASS catalogue to find an initial approximate World Coordinate System (WCS) solution. This solution is then refined by using first IMCORE, to detect sources on the image, and then WCSFIT, to produce the final WCS solution, from the CASUTOOLS package.

IMCORE performs source detection on an image by first computing a low-resolution background image. This is done by estimating background values for 64×64 pixel^2 sections by using an algorithm based on a robust (MAD) iterative $k\sigma$ clipped median. These background values are then filtered to produce the low-resolution background image. Using bi-linear interpolation, the local sky background of every pixel in the original image can then be derived. To identify a source, the algorithm searches for a connected series of six pixels with values higher than a user-specified threshold above the background. For the purpose of astrometry, we want to use as many stars as possible; therefore, we use a low limit of 2σ above the background sky level to detect sources.

WCSFIT uses the initial WCS solution to further correct each image's WCS solutions for translations, skews, scales, and rotations by cross-matching the sources from IMCORE with the Gaia Data Release 1 Catalogue (Gaia Collaboration et al. 2016).

3.3 Catalogue generation

For each FOV that is observed (i.e. each target), the pipeline requires an input catalogue with the RA and Dec. of the stars on which to extract aperture photometry data for each image. This catalogue is generated from a stacked image produced from 50 images in the middle of the night (in order to reduce the airmass and sky background), taken on a target's first night of observation. We have a unique catalogue for each FOV, which is then referenced across all the subsequent nights that target is observed in order to track these stars over long periods of time. This catalogue is cross-matched with *Gaia* Data Release 2 (Gaia Collaboration et al. 2018) to apply proper motion corrections on a night-by-night basis. There is also the facility to cross-match with other catalogues, such as 2MASS (Skrutskie et al. 2006).

The IMSTACK and IMCORE programs from the CASUTOOLS package (Irwin et al. 2004) are used in generating this catalogue. For each of the 50 science images, IMSTACK aligns (using the WCS solutions from WCSFIT) and stacks these images to produce the final stacked image.

IMSTACK defines a WCS reference grid using the first image and subsequent images are then aligned and resampled on to this grid. The σ-clipped mean of the pixel values from all images, scaled by their exposure times, is computed and recorded in the output stacked image. Outliers (defined by threshold values of 5σ) are removed from the averaging. IMSTACK uses a bi-linear interpolation approach where an input pixel is divided into the four pixels on the output grid that surround the input equatorial position, as this can reduce systematic errors (Mighell 1999). The fraction in each output pixel corresponds to the amount of overlap of the input pixel. The final stacked images are crucial in the creation of the catalogues that define each FOV. Therefore, quality checks implemented by the automatic pipeline help to ensure the stacked image is created on a night with good seeing and atmospheric conditions, and ideally no defocusing, to increase the accuracy of the source positions on the field.

IMCORE then performs source detection on the stacked image to create a catalogue of the stars in the FOV. This time, however, IMCORE searches for sources with more than six contiguous pixels containing counts 8σ above the background sky level. This higher threshold limits the detected objects to $I + z'$ magnitudes brighter than ∼21. The background sky level present in the stacked image will vary depending on the angular proximity and phase of the moon; however, we do not see any noticeable variation in the number of stars in the catalogue corresponding to the moon cycle, potentially due to the small pixel size of our CCDs.

3.4 Aperture photometry

IMCORELIST, a fourth CASUTOOLS program, is used to perform aperture photometry on each science image. It carries out essentially the same process as IMCORE but requires an input list of equatorial positions, provided by the catalogue, to define the positions of the apertures. IMCORELIST takes photometric measurements of each source on every image for 13 apertures sizes which are multitudes of the user-defined radius RCORE (default four pixels or 1.4 arcsec).[4] The final aperture for a given night is chosen to balance minimizing the 'average spread' and correlated noise in the target's final differential light curve. The 'average spread' of the target's differential light curve is defined to be the average standard deviation inside 5-min bins. We chose to minimize the rms inside the bins multiplied by the rms of the binned light curve to avoid minimizing genuine photometric structure in the light curve (e.g. stellar variability), whilst also avoiding adding correlated noise in the light curve, for example, from the changing full width at half-maximum (FWHM) and airmass during the night if we choose an aperture that is too small.

4 DIFFERENTIAL PHOTOMETRY

Differential photometry is a technique based on the assumption that stars of similar brightness and colour in an FOV will experience a common photometric pattern, due to shared atmospheric and instrumental effects. For the SSO, we developed an algorithm to automatically choose and combine multiple comparison stars to ensure that the final differential light curves would be reproducible and to avoid the time-intensive, manual selection of stars and potential observer bias. Statistically, it is optimal to use as many stars as possible, weighted appropriately, to reduce the noise levels in the final differential light curves. The algorithm implemented in our pipeline is based on a concept described in Broeg, Fernández & Neuhäuser (2005). This iterative algorithm automatically calculates an 'artificial' comparison light curve (ALC) by weighting all the comparison stars accounting for their variability, and removing those that are clearly variable. To optimize our pipeline for SSO data, several major changes from the algorithm developed by Broeg et al. (2005) were implemented. The basic algorithm is described at the beginning of Section 4.1, while our implemented changes are described in Sections 4.1.1 to 4.1.4. A demonstration of the

[4]The 13 apertures used are multiples (1/2, $1/\sqrt{2}$, 1, $\sqrt{2}$, 2, $2\sqrt{2}$, 4, 5, 6, 7, 8, 10, and 12) of RCORE.

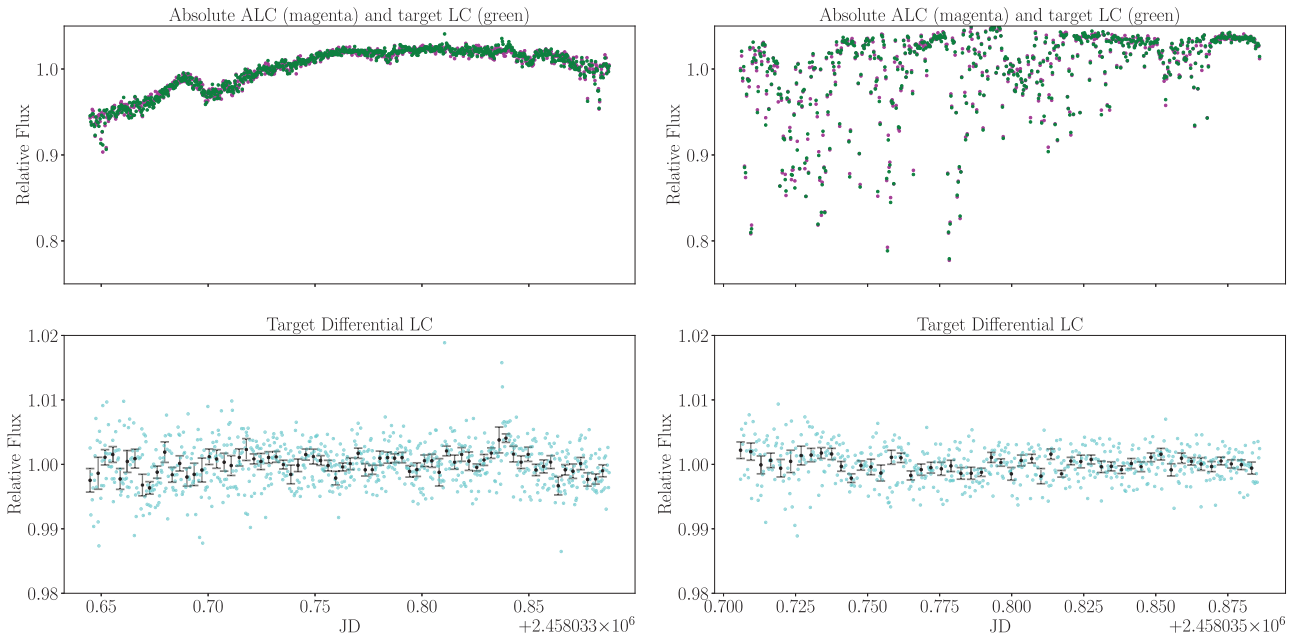

(a) Clear night, 2017 October 6. (b) Cloudy night, 2017 October 8.

Figure 2. Demonstration of the differential photometry algorithm on a bright M8V ($J = 10.4$ mag) target star, observed by Europa during its commissioning phase, comparing the results on a relatively clear night (panel a), and a cloudy night (panel b). The top panels show the ALC (magenta) compared to the target's absolute light curve (green); for both nights, the optimal aperture is 11.3 pixels. The bottom plots show the target's final differential light curve (unbinned points in cyan and 5-min binned points in black), produced by dividing the target's absolute light curve by the ALC. The differential light curve for panel (a) shows a small flare-like structure (JD 2458033.84), which would be difficult to extract from the absolute light curve.

need for differential photometry and the correction with the ALC on observation nights of different quality is shown in Fig. 2.

4.1 Generating an 'artificial' comparison star

The following method is similar to that described in Broeg et al. (2005) where each object (excluding the target and any saturated stars), i, is assigned a weight, $W_{\mathrm{var},i}$, determined by its variability.

(i) The initial weights are defined as

$$W_{\mathrm{var},i} = 1/\sigma^2_{\mathrm{photon},i}. \quad (1)$$

where $\sigma_{\mathrm{photon},i}$ is the photon noise of star i; therefore, in this step, $W_{\mathrm{var},i}$ is set to be equal to the average flux for each object. These weights are normalized such that they sum to 1.

(ii) The ALC is constructed from the weighted mean of the normalized flux (F) of each of the n objects in the field, at each frame j:

$$\mathrm{ALC}_j = \frac{\sum_{i=1}^{n} W_{\mathrm{var},i} F_{ij}}{\sum_{i=1}^{n} W_{\mathrm{var},i}}. \quad (2)$$

(iii) Every star's absolute light curve, F, is divided by this ALC to produce a differential light curve.

(iv) The weight for star i is replaced by

$$W_{\mathrm{var},i} = 1/\sigma_i^2, \quad (3)$$

where σ_i is the standard deviation of the differential light curve for star i.

Stages (ii)–(iv) are repeated with these new weights until the weights are constant to within a threshold of 0.000 01.

4.1.1 *Initial variability cut*

From testing, it became clear that if there was variability in the brightest stars, which are highly weighted during stage (i) of this algorithm, then the initial ALC estimate would be significantly affected. If these objects are not removed, in the next iteration, they would weight down stable stars and weight up those with any similar time variability structure. This results in a runaway effect, downweighting the more stable comparison stars. Therefore, we simply included a variability check prior to generation of the initial ALC by σ-clipping across all stars' normalized light curves for each frame. If any object has >20 per cent of its values clipped, it is determined that this object is variable, and it is removed.

4.1.2 *Colour*

By design, the SSO's targets are usually among the reddest stars in the FOV, and so there is always a colour mismatch between the target star and the comparison stars (see Fig. 3), resulting in second-order differential extinction effects. The redder comparison stars in the field are often significantly dimmer than the target. We therefore resisted the temptation to implement a strict cut of the bluest (and brightest) stars, which would increase the noise in the ALC, and subsequently the target's differential light curve. Instead, we decided to correct the differential extinction in a later stage of the pipeline (see Section 5).

4.1.3 *Distance*

Due to spatially varying atmospheric and optical effects, we added an additional weight based on projected distance from the target

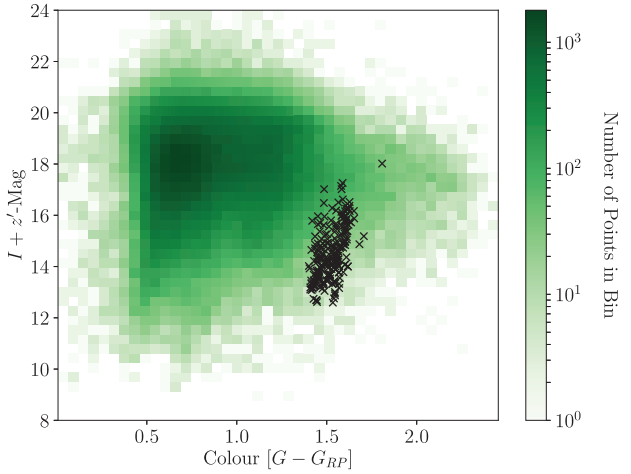

Figure 3. $I+z'$ magnitude against *Gaia* colour, $G-G_{\rm RP}$, for all catalogued stars in every observed FOV (on all telescopes) since 2017 April. The SSO targets are marked by black crosses.

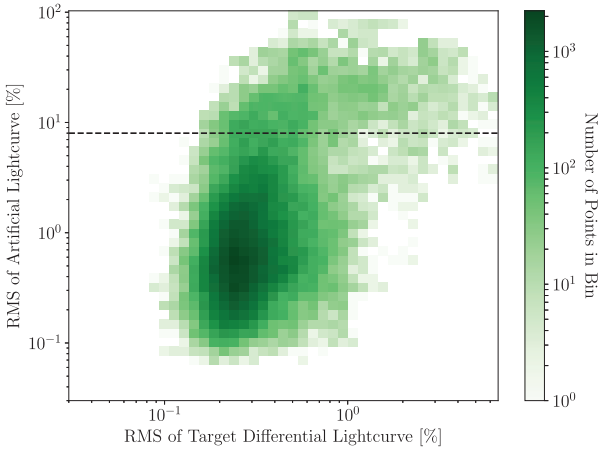

Figure 4. Local rms of unbinned artificial light curves (ALC) against local rms of unbinned target differential light curves for all of Io's observations since 2019 January 1. For this analysis, there is no water vapour correction or removal of cosmic hits, flares or variability, which may cause a points at low ALC rms but a high target light curve RMS of a few per cent. It is clear there is an much larger variation in quality of the target differential light curves when the local rms of the ALCs exceeds the threshold of ∼8 per cent, shown by the black dashed line.

star, using the formula

$$W_{\mathrm{dist},i} = \frac{1}{1+\left(\frac{as_i}{s_{\max}}\right)^2}, \tag{4}$$

where $W_{\mathrm{dist},i}$ is the distance weight of star i, s_i is its separation from the target star, $s_{\max}$ is the maximum distance of any star from the target, and a is a parameter optimized for each night. We chose this form to be finite and relatively flat near the target object and decay slowly as the distance on sky increases. The value of a is chosen to minimize the 'average spread' of the target's differential light curve (as defined in Section 3.4). We normalize these weights to sum to 1, and combine the distance weights and the variability weights from Section 4.1, $W_{\mathrm{var},i}$, to produce the final weights used in the ALC:

$$W_i = W_{\mathrm{var},i}\, W_{\mathrm{dist},i}. \tag{5}$$

Once again, we normalize these weights, which then replace the weights in step (iv) of the iteration process.

4.1.4 Removal of the faintest stars

Ideally, we would use as many comparison stars as possible (weighted appropriately); however, we found that including a large number of faint comparison stars tends to increase the noise in the ALC. It is particularly clear on nights where the atmospheric transmission varies by more than 30 per cent, suggesting passing clouds or poor weather conditions which limit our ability to conduct precise photometric measurements. It was therefore necessary to include a threshold that could be adjusted each night, to remove a certain number of faint stars. This threshold value is chosen automatically to minimize the 'average spread' of the target's final differential light curve (as defined in Section 3.4).

4.2 Night and global light curves

Rather than treating every night of data independently, we can perform the previous differential photometry process (see Section 4.1) on longer duration photometric time-series. This allows us to study photometric variability and rotation over periods of time longer than a night.

To create the global light curves, we apply the differential photometry algorithm to the entire time-series at once, which can span several nights, weeks or months. To ensure any observed changes in flux between nights are caused by real astrophysical variability (and not as a consequence of the differential photometry process), we use the same comparison stars, weightings, and aperture across all nights. This decision, however, reduces our ability to optimize per night, which may result in residuals in the target's final differential light curve, which are particularly obvious on nights with sub-optimal observing conditions.

Choosing the optimal aperture for the global light curves is not a straightforward process. The optimal aperture changes from night to night, mostly due to seeing variations affecting the FWHM of the point spread function (PSF) of sources on the FOV. In practice, the optimal aperture of the series has to be large enough to avoid loosing stellar flux on the nights with larger seeing. This, however, tends to increase the background noise, which disproportionately affects the faintest stars. This effect is mitigated by the cut we implemented on the faintest stars (see Section 4.1.4).

4.3 Bad weather flag

'Bad weather' in the context of the pipeline is defined as the point at which the observing conditions of the night have a significant impact on the target's differential light curve. It is not related to any specific external monitoring of the weather. While, in theory, the ALC should allow us to correct for any change of atmospheric transmission, empirically there is a practical limit to this assumption. We found there was a threshold for the local rms of a data point in the ALC, above which the local rms of the corresponding data point in the target's differential light curve increased dramatically. The local rms of a given data point in the light curve is defined as the rms measured when considering a time range (or box) of ±0.005 d (∼7.2 min) around that point in time. Combining many nights of data allowed us to determine a threshold of 8 per cent to flag (not remove) bad weather in the light curves (see Fig. 4).

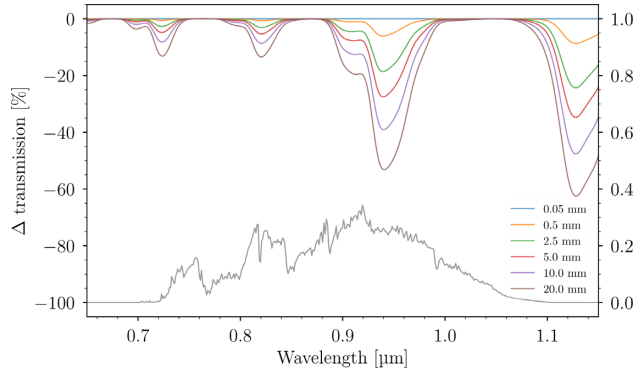

Figure 5. Percentage change in atmospheric transmission (left-hand axis) at different increases of PWV (from 0.05 mm) and, in grey, the spectrum of TRAPPIST-1 as observed through the SSO's $I+z'$ filter, taking into account the overall system efficiency (right-hand axis), as described in Delrez et al. (2018).

5 TELLURIC WATER VAPOUR

SPECULOOS faces additional photometric challenges to most other ground-based transit surveys, as we are observing very red objects in the near-IR. For the vast majority of our observations, we use the $I+z'$ photometric filter. This wavelength range is strongly affected by atmospheric water absorption lines, and to a much lesser extent by OH radical absorption and emission (airglow) lines. The atmospheric transmission varies strongly with the amount of precipitable water vapour in the Earth's atmosphere (see Fig. 5), which can be measured from the ground. Despite the fact that Paranal is an exceptionally dry site (Chilean Atacama Desert), with a nightly median PWV of ∼2.4 mm and 45 nights a year less than 1 mm of PWV (Kerber et al. 2014), it can experience large variations in PWV. This includes pronounced seasonal variations (Kerber et al. 2010), and variations of up to 20 mm over long time-scales and even as much as 13 mm during a single night of observation (see Fig. 6).

By construction of the SPECULOOS's UCD survey, there is always some mismatch in spectral type (and thus colour) between the target and comparison stars used to perform differential photometry. Since redder wavelengths are more readily absorbed by water than bluer wavelengths, when the amount of PWV in the atmosphere changes then objects of different spectral types (whose spectral energy distributions peak at different wavelengths) will experience differing amounts of atmospheric absorption (see Fig. 7). Temporal variations in PWV can therefore imprint second-order extinction residuals on the target differential light curves during differential photometry of the order of ∼1 per cent (Baker, Blake & Sliski 2017) or more, when the change in PWV is significant. These residuals can be a serious limitation for sub-millimag precision surveys, especially as they are of the same order of amplitude as the transit signals we are looking for.

In order to differentiate the photometric variations in the differential light curves related to changes in PWV from those of astrophysical origin, we implemented a correction as part of the automatic pipeline. First, we needed access to accurate, high-cadence PWV measurements, which are provided by Low Humidity and Temperature PROfiling radiometer (LHATPRO). LHATPRO is a microwave radiometer optimized for measuring PWV (from 0 mm to a saturation value of 20 mm, within an accuracy of ∼0.1 mm and with internal precision of 30 μm) situated on a platform at the Very Large Telescope on Cerro Paranal (Kerber et al. 2012).

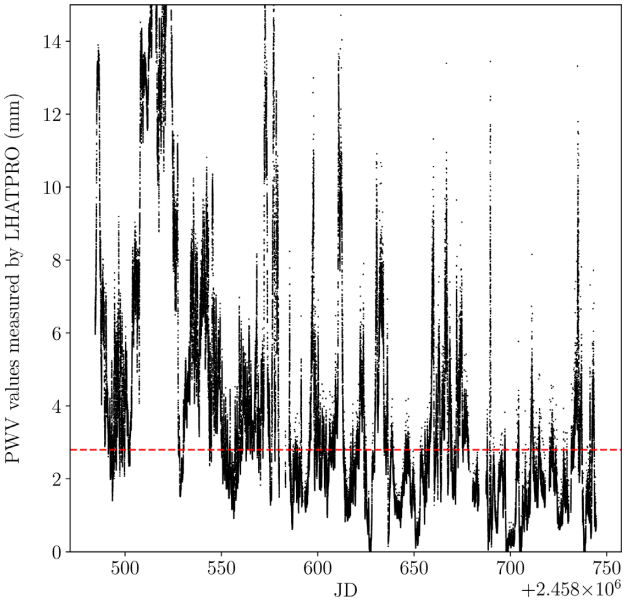

Figure 6. PWV variations in Paranal, measured by LHATPRO from 2019 January 1 to September 18. The median value of 2.795 mm is shown by the dashed red line.

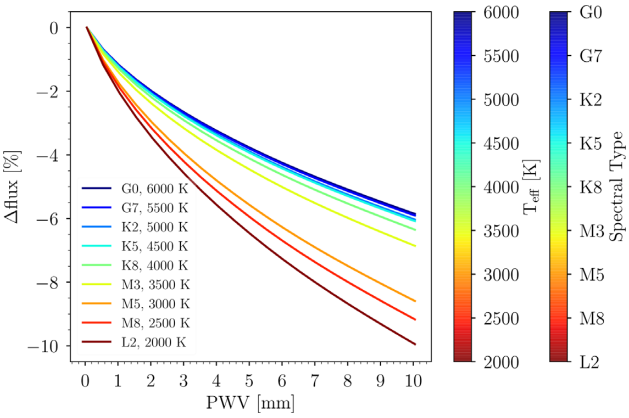

Figure 7. Demonstration of the differential flux effect in the $I+z'$ band with changing PWV. For example, an M8 target star will experience a 9 per cent flux drop for a PWV change from 0.05 to 10 mm, whereas G- and K-type comparison stars (the difference is minimal between hotter stars) will only experience a 5–6 per cent flux decrease.

The LHATPRO instrument measures the column of water vapour at zenith approximately every 2 min, performs a cone scan at 30° for 2.5 min every 15 min and a 2D all-sky scan for 6 min every 6 h. Due to this cone scan, there are peaks in the PWV, which we remove, creating small gaps and discontinuities in the PWV measurement. We use a cubic spline to interpolate between the remaining PWV values to get a smooth light-curve correction. As the gaps are on such a small time-scale (of the order of ∼5 min), we do not see it as a concern to the correction. By using these PWV values, we can then model the effect of the atmospheric absorption with high time resolution on objects of different spectral types (Section 5.1). This allows us to correct for the differential PWV effect between the target and comparison stars (Section 5.2).

5.1 Calculating the effect of varying precipitable water vapour on different spectral types

To model the effect of the PWV on differential light curves, we calculate its 'expected' effect on our measurements for objects of different spectral types, observed with the $I + z'$ filter, at different values of PWV and airmass:

$$f_{I+z'} = \int W(\lambda, X, V)\, R_{I+z'}(\lambda)\, S(\lambda, T_{\rm eff})\, {\rm d}\lambda, \quad (6)$$

where $W(\lambda, X, V)$ is the water absorption spectrum at airmass X and precipitable water vapour V, $R_{I+z'}$ is the instrument response (including the bandpass for filter $I + z'$, CCD quantum efficiency, CCD window, and reflectivity of the mirror coatings), and $S(\lambda, T_{\rm eff})$ is the synthetic stellar spectrum generated from PHOENIX (Husser et al. 2013). This stellar spectrum is dependent on the surface gravity, metallicity, and effective temperature $T_{\rm eff}$ of the star. For simplicity, we assumed stars with solar metallicity ([Fe/H] = 0).

The water absorption spectrum is provided by the SkyCalc Sky Model Calculator, a tool developed by ESO and based on The Cerro Paranal Advanced Sky Model (Noll et al. 2012; Jones et al. 2013). This tool provides a library of atmospheric transmission curves for a continuous range of airmass values and discrete PWV values of 0.05, 0.1, 0.25, 0.5, 1.0, 1.5, 2.5, 3.5, 5.0, 10.0, 20.0 and 30.0 mm. We interpolate between these value to create a smooth 4D grid of all possible values of PWV, airmass, $T_{\rm eff}$, and $f_{I+z'}$, which can be used to correct any object's differential light curve in any frame.

5.2 Applying PWV correction to differential light curves

To correct a target differential light curve from the effect of PWV, we need to compute its effect on both the target and the artificial reference star. For this purpose, we estimate an effective stellar temperature for the artificial reference star from a weighted mean of the temperatures (extracted from *Gaia* DR2) of all the comparison stars in the field, using the weights computed by the pipeline in Section 4.1. The fact that we estimate the temperature of the artificial reference star, and not all of the comparison stars will have a corresponding *Gaia* DR2 temperature, will have little effect on the correction as most of the calibration stars are G and K types. The differential effect between these spectral types is marginal, even for large changes of PWV (see Fig. 7).

Having a correct estimate of the target's effective temperature is more critical. Inaccuracies in this temperature can lead to over, or under, corrections. *Gaia* does not provide reliable values for stellar effective temperatures below 3000 K (Andrae et al. 2018; Dressing et al. 2019); therefore, for every target in our target lis,t we carefully estimate its temperature by calculating the absolute H-magnitudes for our targets from 2MASS and *Gaia* and using the $T_{\rm eff}$–magnitude relation in Filippazzo et al. (2015). These temperature estimates are used as input parameters for the pipeline to compute the effect of the PWV changes on each target's photometry. Finally we divide the PWV effect on the target by the PWV effect on the ALC to generate a differential PWV effect. Then we can correct the target's differential light curve by dividing by this differential PWV effect.

5.3 Impact and statistics of the PWV correction

Correction of the PWV effect is a prerequisite to obtain precise differential photometry and to detect shallow transits. This effect impacts the light curves over both short (single-night) and long (multi-night) time-scales. During observation of a single night,

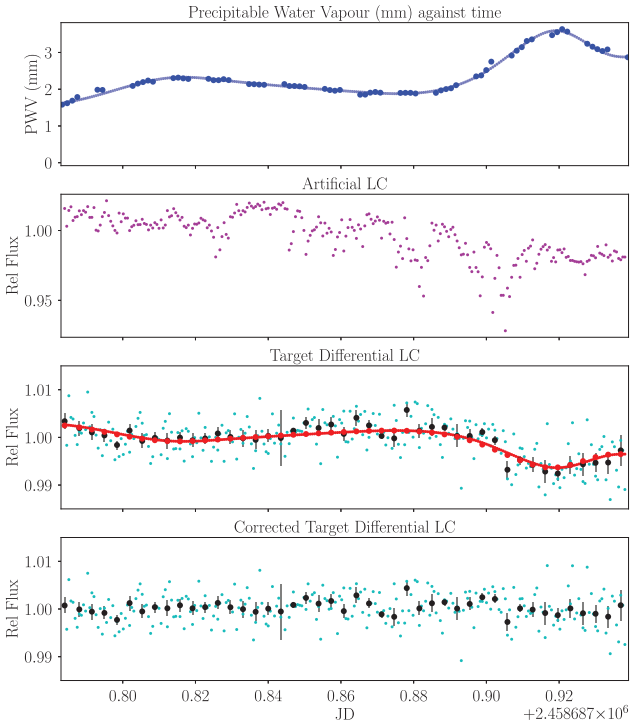

Figure 8. Top panel: PWV (mm) measurements from LHATPRO for the night of 2019 July 22, with peaks removed. The cubic spline interpolation is shown by the blue line. Upper middle panel: the artificial light curve generated for this night. Lower middle panel: Unbinned differential light curve (cyan), with 5-min binned points (black), for an M7-type target. A transit-like feature is visible at the end of the light curve. The expected differential flux effect of PWV is shown in red. Bottom panel: The corrected differential measured light curve in cyan and 5-min binned points in black. We obtain this light curve by dividing the original differential light curve by the calculated differential flux effect from PWV. The transit-like feature was due to PWV changes and is no longer visible in the corrected light curve.

residuals in the target differential light curves may mimic a transit-like signal, even with modest PWV variations of ∼1 mm (see Fig. 8).

By analysing all the PWV measurements from our first year of operation, we can estimate the likelihood of observing a corresponding differential flux effect large enough to be mistaken for a transit. By averaging the PWV values in hour bins (typical time-scale of a transiting planet), the variations between consecutive bins will result in a calculable differential flux effect, for an example 2650-K target (M7V) and 4600-K (K4V) artificial light curve. From the cumulative histogram of these differential flux effects (see Fig. 9), we can approximate that we would have a 95 per cent chance of observing at least one flux variation (δF) larger than x, using

$$P(\delta F \leq x)^n = 0.05, \quad (7)$$

where n is the number of flux variations ($n + 1$ hour bins) and $P(\delta F \leq x)$ is the probability of observing a flux variation less than x. We estimate that we would have a 95 per cent chance of seeing at least one amplitude variation of ∼1 mmag every night, ∼4 mmag every month, and ∼8 mmag every year. While these larger variations in the light curves may not always resemble transits, they are significant enough to affect our detection of a transit, demonstrating the need for our implemented correction. Over multiple nights of observation, correcting for this effect is an absolute necessity to isolate intrinsic variability of our targets from atmospheric transmission changes due to variation of PWV from one night to another (see Fig. 10).

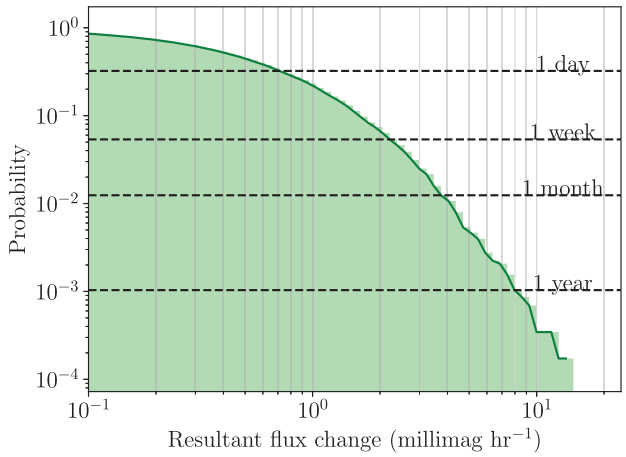

Figure 9. Cumulative histogram of the amplitude change in a target's differential light curve induced by PWV variation on typical transit time-scales (1 h). We record PWV variations between consecutive 1 hr bins from 2019 January 1 to September 18 and used these variations to generate the corresponding differential flux variations for a 2650-K target object and 4600-K comparison star. We calculate the amplitude variations that we have a 95 per cent chance of seeing at least one of on a daily (±0.7 mmag), weekly (±2 mmag), monthly (±4 mmag), and annual (±8.1 mmag) time-scale, marked by the dashed black lines.

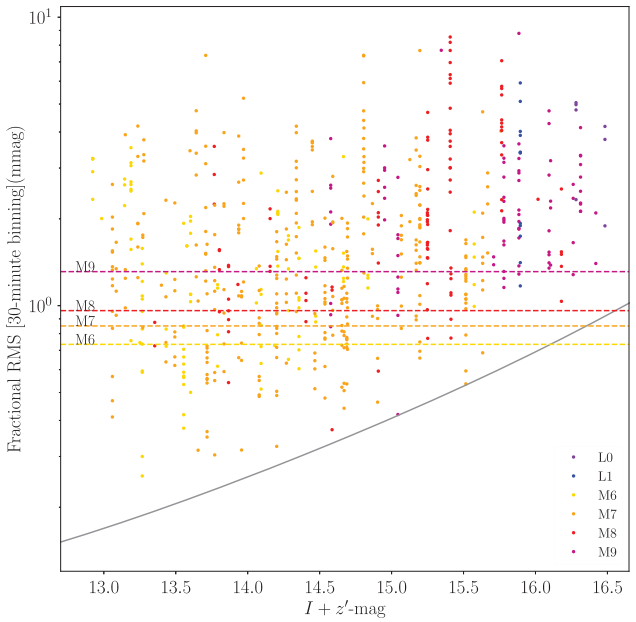

Figure 11. Fractional rms (for 30-min binning) of all the SSO's UCD target light curves carried out with $I + z'$ filter from 2019 January 1 to September 18. There is a data point for each target on each night of observation – the vertical lines correspond to different fractional rms on different nights of observation for the same target. The noise model for the best possible observing conditions is shown in grey. The dashed lines show the minimal level of precision needed to detect a single transit of a TRAPPIST-1b-sized planet (1.127 $R_\oplus$) around stars of different spectral types at 9σ.

6 PHOTOMETRIC PERFORMANCE OF THE SSO

The ability of our automatic pipeline to provide consistent and reproducible results allows us to carry out daily monitoring of the photometric performance and health of the overall system.

6.1 Typical photometric precisions of SSO light curves

To illustrate the typical photometric performances of the facility, and its capability to detect single transits of Earth-size planets, Fig. 11 displays the measured fractional rms (for 30-min bins) for the SSO target light curves, obtained each night of observation. To ensure there were at least five bins for each light curve, we only included light curves where there was more than 150 min of total exposure. This accounts for 98 targets and 179 combined nights of observations with multiple telescopes from 2019 January 1 to September 18. The binning time-scale we adopted to compute the rms is set to match the typical transit duration of a short-period planet orbiting an UCD.

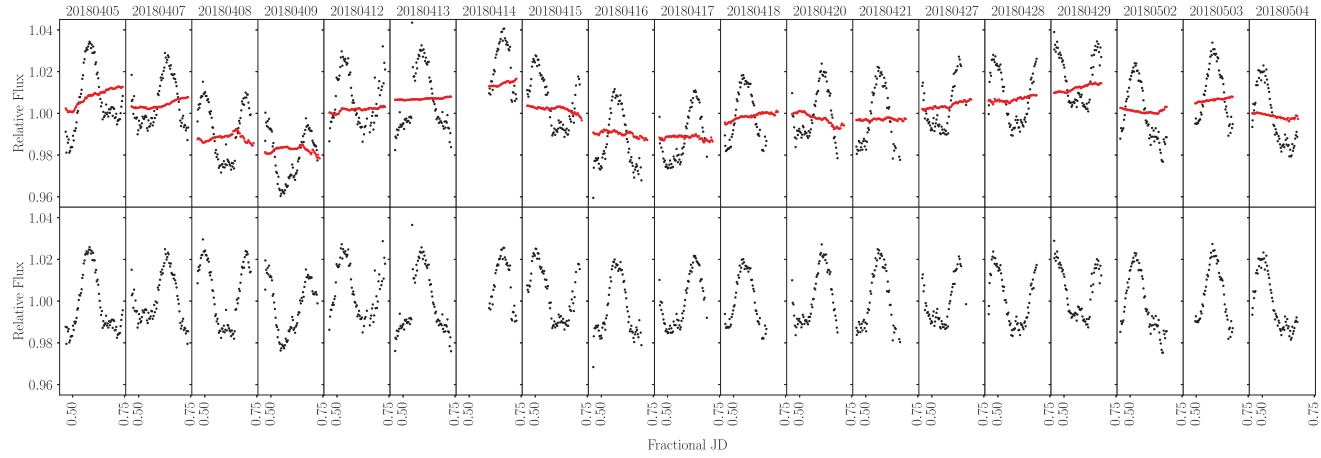

Figure 10. Top panel: global $I + z'$ 5-min binned differential light curve for an M8-type variable target (LP 609-24, $J = 12.33$ mag) is shown in black, observed from 2018 April 5 to May 6, during the commissioning phase of Callisto. The calculated differential flux effect from PWV is shown in red (5-min binned). This target exhibits both nightly and multi-night variability. Bottom panel: wate-vapour-corrected differential light curve (5-min binned). While the night-to-night variability remains, the longer time-scale variations were a result of the PWV changes between nights and were removed during the PWV correction.

This figure demonstrates that for quiet targets on nights with good observing conditions we are reaching the best possible precision, as determined by our noise model. This noise model (Merline & Howell 1995) accounts for several different contributions: Poisson noise from the star, read noise from the detector, noise from background light, noise from dark current, and atmospheric scintillation. For the atmospheric scintillation, we use a modified form of Young's approximation, specific for Paranal (Osborn et al. 2015). The targets we observe typically have exposure times from 10 to 60 s; therefore, we assume the noise model for 60-s exposure, with an overhead of 10.5 s, which gives 25 data points in each 30-min bin. The noise model illustrated in Fig. 11 is also assumed for an aperture of 11.3 pixels on the best possible night, with an airmass of 1 and a background sky level of 49.04 ADU pixel^{-1} (the lowest recorded sky background since 2019 January).

There is no correction for photometric variability, removal of bad weather, or selection of the nights with the best observing conditions. This results in the vertical stripes for each target corresponding to large spreads in rms in the light curves for different nights, related to the wide range of observing conditions and potentially that target's intrinsic variability. This spread can be seen to limit our single-transit detection efficiency, thereby demonstrating the need to remove photometric variability. We expect the median precision we find (and our detection potential) to improve when the stellar variability is properly accounted for, which will be presented in a future paper.

The photometric precisions reached by our least active targets in this diagram show that we are reaching sub-millimag precisions for approximately 30 per cent of light curves (with a median precision of ∼1.5 mmag), and up to ∼0.26 mmag for the brightest objects. In Fig. 11, we superimposed an approximation of the minimum photometric precision required to measure a single transit by a TRAPPIST-1b-sized planet (1.127 $R_\oplus$) with an S/N of 9 for different spectral types (Pecaut & Mamajek 2013). This demonstrates SSO's excellent quality and detection capability, especially for quiet targets observed on nights with good observing conditions.

6.2 Simultaneous observation comparison with *TESS*

NASA's *Transiting Exoplanet Satellite Survey* (*TESS*; Ricker et al. 2015) was launched in 2018 April. While *TESS* is optimized for detecting planets around G- to mid-M-dwarf stars, their wide bandpass allows them to additionally observe the brightest late M-dwarfs with high precisions.

Here we present a comparison of a night of simultaneous observation of the M6 star, WOH G 618 (TIC 31381302, J = 10.3 mag, T = 12.5 mag, $I + z'$ = 12.6 mag), by a single SSO telescope to *TESS* data (Fig. 12). For *TESS*, we include both the publicly available 2-min cadence data and the final light curve from the MIT Quick Look Pipeline (QLP). The QLP was developed to extract light curves specifically for targets in the 30-min full frame images (FFIs). It is shown here as an example for FFI photometry, allowing us to gauge the precision that can be achieved for targets that are not part of *TESS*' 2-min sample. The QLP and other custom pipelines can be used to extract light curves from the FFIs for the majority of late M-dwarfs in the *TESS* fields.

We see excellent agreement between the three data sets. There remains a structure in the SSO-*TESS* QLP residuals that appears to correlate with the variability; however, this is within error. The SSO light curve shows less white noise than *TESS*, as expected, because *TESS* is not optimized for these very red objects. For fainter and redder UCDs, we expect that the quality of the SSO light curves will exceed *TESS*; however, for the brightest SPECULOOS targets, the light curves will be comparable. We believe this demonstrates the remarkable performance of both *TESS* and SSO, especially considering the detection potential when combining simultaneous observations from multiple SSO telescopes and *TESS* together.

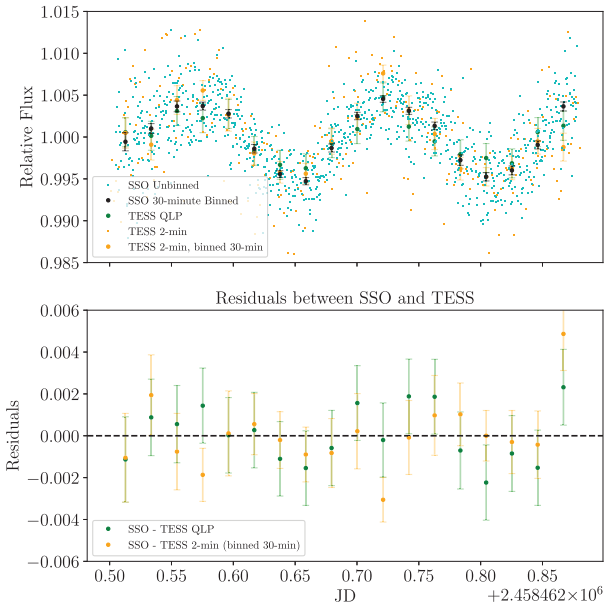

Figure 12. Top panel: SSO's differential light curve compared to the light curves from *TESS* 2-min cadence data and MIT QLP 30-min cadence data for an M6V object (J = 10.3 mag) on 2018 December 10. Bottom panel: the residuals between the *TESS* and SSO light curves.

7 DISCUSSION AND PERSPECTIVES

This paper illustrates a practical and successful implementation of an automated differential photometry algorithm with carefully calibrated weighting schemes for comparison stars, and a correction of the effect of varying telluric water vapour. The analysis of the photometric performance of SSO's first year of operation shows that, with these methods, we can regularly reach sub-millimag precision photometry, for our quieter targets.

Several publications have already addressed this telluric water vapour problem when observing cool stars in the near-IR (Bailer-Jones & Lamm 2003; Blake et al. 2008; Blake & Shaw 2011). The MEarth survey has a similar 715–1000 nm bandpass and also witnessed induced photometric systematics that could mimic an exoplanet transit, due to variations in atmospheric water vapour (Berta et al. 2012). These systematics were also a limiting factor in the type of M-dwarfs (>0.15 $R_\odot$) that could have rotation periods extracted from MEarth (Newton et al. 2018). Despite identification of the issue, we have not found any implemented correction of telluric water vapour, directly from the first principles, for a large-scale survey in the literature. However, we do note that MEarth developed an alternative method of correcting the water vapour effect (Irwin et al. 2011), by medianing all M-dwarf light curves gathered by their eight telescopes (at each site) in half-hour time bins to create a 'common mode' light curve. They then calculate a scaling factor for each star, determined by a least-squares optimization. While this method has proved successful to a survey like MEarth (Berta et al. 2011), which observes dozens of stars every 30 min,

for SSO, which only ever observes a maximum of four M-dwarf targets at once, this technique is limited. We believe that correcting the water vapour from the transmission spectra directly offers the advantage that it is determined from an independent data set (LHATPRO), and removes the chance of overfitting real structure.

It was therefore necessary to develop a model to correct for this differential effect. Additionally, this work highlights how beneficial it is to have access to high time resolution, high-precision PWV measurements. This correction, however, has a wider impact than just the correction of the SSO light curves. It could be applied to any future transit survey observing redder stars in the near-IR, including earlier M dwarfs, or more generally, for example, in long-term photometric variability studies of red objects.

Not every facility has access to expensive water vapour radiometers and so there has been substantial development of alternate methods of measuring the PWV. Instruments like aTmCam (Li et al. 2012, 2014) and CAMAL (Baker et al. 2017) use a set of imagers to take simultaneous observations of bright calibration stars with different narrow-band filters chosen to be in band and out of band for water. Along with measurements of local surface pressure and temperature, GPS receivers have also been used to estimate the atmospheric PWV to accuracies of 0.11–1 mm (Bevis et al. 1992; Duan et al. 1996; Blake & Shaw 2011; Castro-Almazán et al. 2016; Li et al. 2018). We have shown in this paper that changes in PWV of 1 mm are sufficient to limit our detection efficiency and can even mimic a transit from an Earth-sized planet, so accurate PWV measurements are essential. As an alternative to correcting the effect, it is possible to minimize the impact of water bands in the near-IR (and the photometric consequences from changing PWV) by reducing the filter band-pass, but at the cost of losing stellar photons and the need for a larger telescope.

We have identified a couple of limitations in our PWV correction, which could potentially leave some residual structures in the final differential light curve. The LHATPRO instrument saturates at 20 mm at zenith which will limit the accuracy we can achieve for very high PWV, especially for high airmass. There is also an ∼200-m vertical distance between the VLT platform (2635 m) and the SSO facility. Additionally, the LHATPRO instrument measures the water vapour at zenith instead of along our line of sight. All of these factors may result in underestimating the amount of PWV affecting our observations. The effect on our photometry is, however, likely to be small; Querel & Kerber (2014) found that PWV over Paranal was spatially homogeneous down to elevations of 27°.5, such that measuring PWV along zenith is sufficient for most astronomical applications. Concerningly, this homogeneity was found to decrease with rising levels of water in the atmosphere, as they found the PWV variations were reliably 10–15 per cent of the absolute PWV. Therefore, our correction is likely to be most effective at zenith where we do not have to consider spatial variations, and more effective at low values of PWV (<2 mm), where the variations across the sky are of the order of ∼0.1–0.3 mm. An investigation of the impact from these various effects on our precise photometry is planned for the future.

As mentioned in Section 6.1, stellar variability can seriously limit our planet detection efficiency. Future development of the pipeline will essentially focus on the implementation of an algorithm to identify and model flares and variability simultaneously with an automatic transit search. By optimizing our detection efficiency, SPECULOOS provides a unique opportunity to explore the planetary population around UCDs, matching space-level photometric precisions with an ability to study fainter and redder objects than ever before.

ACKNOWLEDGEMENTS

The research leading to these results has received funding from the European Research Council (ERC) under the FP/2007–2013 ERC grant agreement no. 336480, and under the H2020 ERC grant agreements 679030 and 803193, and from an Actions de Recherche Concertée (ARC) grant, financed by the Wallonia–Brussels Federation. This work was also partially supported by a grant from the Simons Foundation (PI Queloz, grant number 327127), as well as by the Mobilising European Research in Astrophysics and Cosmology (MERAC) Foundation (PI Triaud). LD acknowledges support from the Gruber Foundation Fellowship. PI Gillon and EJ are Fonds de la Recherche Scientifique (FRS-FNRS) Senior Research Associates. B-OD acknowledges support from the Swiss National Science Foundation (PP00P2-163967). VVG is a FRS-FNRS Research Associate. MNG and CXH acknowledge support from Juan Carlos Torres Fellowships.

REFERENCES

Andrae R. et al., 2018, A&A, 616, A8
Bailer-Jones C. A. L., Lamm M., 2003, MNRAS, 339, 477
Baker A. D., Blake C. H., Sliski D. H., 2017, PASP, 129, 085002
Berta Z. K., Charbonneau D., Bean J., Irwin J., Burke C. J., Désert J.-M., Nutzman P., Falco E. E., 2011, ApJ, 736, 12
Berta Z. K., Irwin J., Charbonneau D., Burke C. J., Falco E. E., 2012, AJ, 144, 145
Bevis M., Businger S., Herring T. A., Rocken C., Anthes R. A., Ware R. H., 1992, J. Geophys. Res., 97, 15
Blake C. H., Shaw M. M., 2011, PASP, 123, 1302
Blake C. H., Bloom J. S., Latham D. W., Szentgyorgyi A. H., Skrutskie M. F., Falco E. E., Starr D. S., 2008, PASP, 120, 860
Broeg C., Fernández M., Neuhäuser R., 2005, Astron. Nachr., 326, 134
Burdanov A., Delrez L., Gillon M., Jehin E., 2018, in Deeg H., Belmonte J., eds, SPECULOOS Exoplanet Search and Its Prototype on TRAPPIST. Handbook of Exoplanets, Springer, Cham, p. 1007
Castro-Almazán J. A., Muñoz-Tuñón C., García-Lorenzo B., Pérez-Jordán G., Varela A. M., Romero I., 2016, in Peck A. B., Seaman R. L., Benn C. R., eds, Proc. SPIE Conf. Ser. Vol. 9910, Observatory Operations: Strategies, Processes, and Systems VI. SPIE, Bellingham, p. 10
de Wit J., Seager S., 2013, Science, 342, 1473
Delrez L. et al., 2018, in Marshall H. K., Spyromilio J., eds, Proc. SPIE Conf. Ser. Vol. 10700, Ground-based and Airborne Telescopes VII. SPIE, Bellingham, p. 107001I
Dressing C. D. et al., 2019, AJ, 158, 87
Duan J. et al., 1996, J. Appl. Meteorol., 35, 830
Filippazzo J. C., Rice E. L., Faherty J., Cruz K. L., Van Gordon M. M., Looper D. L., 2015, ApJ, 810, 158
Gaia Collaboration et al., 2016, A&A, 595, A2
Gaia Collaboration et al., 2018, A&A, 616, A1
Gardner J. P. et al., 2006, Space Sci. Rev., 123, 485
Gillon M., 2018, Nat. Astron., 2, 344
Gillon M., Jehin E., Magain P., Chantry V., Hutsemékers D., Manfroid J., Queloz D., Udry S., 2011, Eur. Phys. J. Web Conf., 11, 06002
Gillon M. et al., 2016, Nature, 533, 221
Gillon M. et al., 2017, Nature, 542, 456
Gilmozzi R., Spyromilio J., 2007, The Messenger, 127, 11
Gizis J. E., Paudel R. R., Mullan D., Schmidt S. J., Burgasser A. J., Williams P. K. G., 2017, ApJ, 845, 33
Günther M. N. et al., 2019, AJ, 159, 60
Husser T.-O., Wende-von Berg S., Dreizler S., Homeier D., Reiners A., Barman T., Hauschildt P. H., 2013, A&A, 553, A6
Irwin M. J. et al., 2004, in Quinn P. J., Bridger A., eds, Proc. SPIE Conf. Ser. Vol. 5493, Optimizing Scientific Return for Astronomy through Information Technologies. SPIE, Bellingham, p. 411

Irwin J., Berta Z. K., Burke C. J., Charbonneau D., Nutzman P., West A. A., Falco E. E., 2011, ApJ, 727, 56
Jehin E. et al., 2011, The Messenger, 145, 2
Jones A., Noll S., Kausch W., Szyszka C., Kimeswenger S., 2013, A&A, 560, A91
Kaltenegger L., Traub W. A., 2009, ApJ, 698, 519
Kerber F. et al., 2010, in Stepp L. M., Gilmozzi R., Hall H. J., eds, Proc. SPIE Conf. Ser. Vol. 7733, Ground-based and Airborne Telescopes III. SPIE, San Diego, 77331M
Kerber F. et al., 2012, in McLean I. S., Ramsay S. K., Takami H., eds, Proc. SPIE Conf. Ser. Vol. 8446, Ground-based and Airborne Instrumentation for Astronomy IV. SPIE, Bellingham, p. 84463N
Kerber F. et al., 2014, MNRAS, 439, 247
Kirkpatrick J. D., 2005, ARA&A, 43, 195
Kirkpatrick J. D. et al., 2012, ApJ, 753, 156
Lang D., Hogg D. W., Mierle K., Blanton M., Roweis S., 2010, AJ, 139, 1782
Li T. et al., 2012, McLean I. S., Ramsay S. K., Takami H., eds, Proc. SPIE Conf. Ser. Vol. 8446, Ground-based and Airborne Instrumentation for Astronomy IV. SPIE, Bellingham, p. 84462L
Li T., DePoy D. L., Marshall J. L., Nagasawa D. Q., Carona D. W., Boada S., 2014, Ramsay S. K., McLean I. S., Takami H., eds, Proc. SPIE Conf. Ser. Vol. 9147, Ground-based and Airborne Instrumentation for Astronomy V. SPIE, Bellingham, p. 91476Z
Li D., Blake C. H., Nidever D., Halverson S. P., 2018, PASP, 130, 014501
McCormac J., Pollacco D., Skillen I., Faedi F., Todd I., Watson C. A., 2013, PASP, 125, 548
Merline W. J., Howell S. B., 1995, Exp. Astron., 6, 163
Mighell K. J., 1999, in Mehringer D. M., Plante R. L., Roberts D. A., eds, ASP Conf. Ser. Vol. 172, Astronomical Data Analysis Software and Systems VIII. Astron. Soc. Pac., San Francisco, p. 317
Newton E. R., Mondrik N., Irwin J., Winters J. G., Charbonneau D., 2018, AJ, 156, 217
Noll S., Kausch W., Barden M., Jones A. M., Szyszka C., Kimeswenger S., Vinther J., 2012, A&A, 543, A92
Osborn J., Föhring D., Dhillon V. S., Wilson R. W., 2015, MNRAS, 452, 1707
Pecaut M. J., Mamajek E. E., 2013, ApJS, 208, 9
Querel R. R., Kerber F., 2014, in Ramsay S. K., McLean I. S., Takami H., eds, Proc. SPIE Conf. Ser. Vol. 9147, Ground-based and Airborne Instrumentation for Astronomy V. SPIE, Bellingham, p. 914792
Ricker G. R. et al., 2015, J. Astron. Telesc. Instrum. Syst., 1, 014003
Sanders G. H., 2013, J. Astrophys. Astron., 34, 81
Seager S., Deming D., Valenti J. A., 2009, Astrophys. Space Sci. Proc., 10, 123
Skrutskie M. F. et al., 2006, AJ, 131, 1163
Tamburo P., Muirhead P. S., 2019, PASP, 131, 114401
Wheatley P. J. et al., 2018, MNRAS, 475, 4476
Williams P. K. G., Berger E., Irwin J., Berta-Thompson Z. K., Charbonneau D., 2015, ApJ, 799, 192

This paper has been typeset from a TEX/LATEX file prepared by the author.